Hindawi
Geofluids
Volume 2017, Article ID 2595701, 18 pages
https://doi.org/10.1155/2017/2595701

WILEY | Hindawi

Research Article

Simulation and Analysis of Long-Term CO_2 Trapping for the Shenhua CCS Demonstration Project in the Ordos Basin

Ying Yu,[1] Yilian Li,[1] Guodong Yang,[2] Fengcheng Jiang,[1] Sen Yang,[1] and Yongsheng Wang[3]

[1]*School of Environmental Studies, China University of Geosciences, Wuhan 430074, China*
[2]*College of Resources and Environmental Engineering, Wuhan University of Science and Technology, Wuhan 430081, China*
[3]*China Shenhua Coal Liquefaction Co., Ltd. Ordos, Ordos 017209, China*

Correspondence should be addressed to Yilian Li; yl.li@cug.edu.cn

Received 14 July 2017; Revised 21 October 2017; Accepted 12 November 2017; Published 10 December 2017

Academic Editor: Xiaoqing Shi

Copyright © 2017 Ying Yu et al. This is an open access article distributed under the Creative Commons Attribution License, which permits unrestricted use, distribution, and reproduction in any medium, provided the original work is properly cited.

The Shenhua CO_2 capture and sequestration (CCS) project has achieved its goal of injecting 100,000 tons/year CO_2 into the saline aquifers of the Ordos Basin. This study analyzes the geochemical interactions between CO_2, formation fluid, and host rock of the major formations in the Ordos Basin, assesses the CO_2 trapping capabilities, and predicts the final mineral forms of injected CO_2. Reactive transport simulations are performed using a 2D radial model, which represents a homogeneous formation. The results show that 80% of injected CO_2 remains as free supercritical gas in each formation after injection, while most of CO_2 is sequestrated in different carbonate mineral assemblages after 10,000 years. The CO_2 mineral trapping capacities of the Shiqianfeng and Shihezi formations are smaller than the Liujiagou formation. Calcite, dawsonite, and siderite are stable CO_2 trapping minerals, while dolomite, ankerite, and magnesite are not. The increase in porosity and permeability of the three formations in the first 100 years agrees with the observation from the Shenhua CCS Project. Also the decrease in porosity and permeability after 100 years shows agreement with other modelling studies using the similar methods. These results are useful for the evaluation of the geochemical process in long-term CO_2 geological storage.

1. Introduction

The global average surface temperature growing in decades has increased the worries about global warming [1]. The excess emission of greenhouse gas (mainly CO_2) is considered as the principal culprit [2, 3]. Therefore, CO_2 capture and sequestration (CCS) has been proposed—especially CO_2 geological storage (CGS), which becomes one of the most effective methods to mitigate the greenhouse effect [4, 5].

Among CGS studies, the migration patterns of CO_2 and geochemical responses induced by CO_2 injection have been focused on. The results indicate that physical properties of fluid and host rock control the way CO_2 moves, while chemical processes dominate the fate of CO_2 [6–8]. Factors affecting CO_2 migration mainly include the following: (1) density difference of fluid; (2) penetration pathway; (3) capillary pressure; (4) injection rates; and (5) formation pressure [9–11]. However, CO_2 plume beneath caprocks barely moves without injection pressure as driven force, although molecular diffusion/dispersion and convective mixing occur in the CO_2 bearing zone. After injection, the CO_2-water-rock interactions dominate the CO_2 trapping mechanisms, which have great effect on the long-term safety of CO_2 geological storage.

CO_2-water-rock interactions have been widely studied with laboratory experiment and numerical simulation. Several researchers have investigated the reactive transport processes based on field conditions. Cipolli et al. [12] studied the CO_2 injection into the serpentine in Italy by EQ 3/6. Gaus et al. [13] modelled the CO_2 diffusion through the caprock at the Sleipner project using PHREEQC. Audigane et al. [14] simulated the CO_2 injection into a saline aquifer at the Sleipner project using TOUGHREACT. These studies indicate that dissolution of host rock contributes to the CO_2 mineral trapping. The pattern of mineral dissolution and precipitation is different under different field conditions [7, 8, 15].

Some other studies have focused on several specific minerals involved in CO_2-water-rock interactions. Xu et al. [16–18] simulated the CO_2-water-rock interactions using TOUGHREACT; they found dissolution of calcite and aluminosilicate and precipitation of ankerite, dawsonite, siderite, magnesite, calcite, and dolomite. Wigand et al. [19] conducted experiments under in situ conditions of the Bunter Sandstone Formation in Europe and observed dolomite dissolution and smectite precipitation. Okuyama et al. [20] simulated the CO_2-water-rock interactions induced by CO_2 injection in the Tokyo Bay area by TOUGHREACT, and dissolution of plagioclase and precipitation of dawsonite were observed. Their studies indicate that dissolution of carbonate minerals is regarded as dominant reaction in a short time [21, 22]. Meanwhile, precipitation of trapping minerals depends on the primary mineral assemblages [23].

For a specific site or formation, CO_2-water-rock interactions are different due to different hydrogeochemical conditions, which are worth investigating to enhance our understanding of CO_2 evolution in each CGS project. The Shenhua CCS Project has finished its goal of injecting 100,000 tons/year CO_2 into the onshore saline aquifers of the Ordos Basin by the end of 2013, with CO_2 captured from the Shenhua Direct Coal Liquefaction Company [24]. As the first integrated CGS project in China, the Shenhua CCS Project has attracted extensive research interest. Wang [25] and Yang [26] explored the mechanism of reactions between the CO_2 fluid and the Shiqianfeng/Shihezi formation in the Ordos Basin, using a high pressure reactor simulating the underground conditions. Tao [27] investigated the mineralization of CO_2 in the Liujiagou formation using the same equipment. However, experimental studies are limited by time scales, and CO_2 mineral trapping that immobilizes CO_2 permanently is a long-term process.

The objective of this study is to investigate the long-term CO_2-water-rock interactions based on the three formations at the Shenhua CCS site. In addition, pH changes and mineral dissolution/precipitation caused by CO_2 injection are analyzed. The supercritical CO_2 flow and geochemical reactions are modelled by TOUGHREACT, which coupled simulate subsurface multiphase fluid and heat flow, solute transport, and chemical reactions. Furthermore, the simulated geochemical processes in the three formations are compared with other experimental and modelling studies. The results from this study can be useful for the evaluation of long-term CO_2 geological storage and the geochemical process for practical implementations of CCS.

2. Geological Setting

The Shenhua CCS Project is located in the east section of the northern Yishan Slope in the Ordos Basin, which is an ideal place for large-scale CO_2 storage in geological formations in China [28]. The Triassic and Permian sandstone of the Ordos Basin are recognized as deep saline aquifers that have significant potential for CO_2 geological sequestration. The sedimentary thickness is more than 1500 m from Ordovician to Lower Triassic in the study area. Five reservoir-caprock assemblages (Liujiagou, Shiqianfeng, Shihezi, Shanxi, and Majiagou) have been identified according to the previous studies [24, 29]. In this study, the Liujiagou, Shiqianfeng, and Shihezi formations are selected as the target layers for simulations (Figure 1), because they are major formations for CO_2 geological storage at the Shenhua CCS Project [24]. The fractures in the three formations are less developed with minor sizes and have little impact on the CO_2 geological storage [30].

2.1. Formation Characterization. The Liujiagou formation is at depths of 1576–1699 m. The interbedded seal is 5–15 m thick and discontinuous, characterized as silty mudstone or muddy siltstone. The reservoir formation is 123 m thick mainly composed of arkoses and lithic feldspathic sandstone. The porosity and permeability of the reservoir are 6.3–10% and 0.02×10^{-15}–2.81×10^{-15} m^2, respectively [24, 27, 30].

The Shiqianfeng formation is situated at depths of 1699–1990 m. The caprock is 26.2–103.6 m thick and characterized as silty mudstone or muddy siltstone, which is relatively continuous. The reservoir is 292 m thick and mainly composed of floodplain feldspathic quartz sandstone, with porosity and permeability 5–12.9% and 0.1×10^{-15}–6.58×10^{-15} m^2, respectively [24, 25, 30].

The Shihezi formation is located at depths of 1990–2232 m. There is relatively pure mudstone in the upper Shihezi formation as a 116 m thick regional seal. The reservoir is 126 m thick and mainly composed of feldspathic quartz sandstone and feldspathic litharenite. The porosity and permeability of the reservoir are 8.8–12.6% and 1.23×10^{-15}–5.99×10^{-15} m^2, respectively [24, 26, 30].

The details of mineral composition of the three formations and selected secondary minerals are given in Table 1. Considering the availability of kinetic data, we adjust the primary minerals used in the simulations referring to Xu et al. [18, 31]. According to the equilibrium batch modelling and previous studies of CO_2-water-rock interactions [7, 31], almost all the possible secondary minerals are considered in the simulations. The average temperature and pressure gradient of the study area are estimated as 30°C/km and 100 bar/km, respectively.

2.2. Formation Fluid Chemistry. In the Liujiagou formation, the groundwater is dominated by Ca-Na-Cl water type and highly mineralized with a total dissolved solid content (TDS) of 56 g/L. In the Shiqianfeng formation, the groundwater is also dominated by Ca-Na-Cl water type and highly mineralized with a TDS of 31.2 g/L. In the Shihezi formation, the groundwater is dominated by Na-Ca-Cl water type and lowly mineralized with a TDS of 9.39 g/L. The details of aqueous chemical concentrations are given in Table 2 [26, 27, 32].

Before simulating CO_2 injection, batch simulations are conducted to equilibrate the primary minerals with in situ water at the formation temperature and CO_2 partial pressure. The resulting water chemistry is used as the initial aqueous concentrations for reactive transport simulations [18, 33].

3. Simulation Methods

3.1. Governing Equations. TOUGHREACT is a comprehensive nonisothermal multicomponent reactive fluid flow and

Stratum			Group		Thickness (m)	Lithologic section	Lithologic characteristics
Period	System	Series					
Cenozoic	Quaternary				0–30		Grayish yellow gravel layer
Mesozoic	Cretaceous		Luohe		0–137		Sandstone intercalated with mudstone
	Jurassic	Middle	Anding		80–150		
			Zhiluo		200–400		
		Lower	Yanan		250–300		
	Trissic	Upper	Yanchang		790–1415		
		Middle	Zhifang		300–530		
		Lower	Heshanggou		47–169		
			Liujiagou	Upper	202–422		Light brown and off-white middle-fine and coarse sandstone intercalated with brownish yellow and brown silty mudstone and pelitic siltstone
				Middle			Light brown and off-white middle-fine and coarse sandstone intercalated with yellowish-brown, purple brown, blue gray pelitic siltstone
				Lower			Light brown and off-white middle-fine and coarse sandstone intercalated with yellowish-brown, purple brown, blue gray silty mudstone
Upper Paleozoic	Permian	Upper	*Shiqianfeng*	Upper	200–345		Purplish red and brick red mudstone mixed with thin limestone or nodule layer
				Lower			Light grayish green, yellowish green, grayish purplish red feldspathic quartz sandstone mixed with purplish red silty mudstone and grayish green pelitic siltstone and mudstone is intercalated with sand lens
			Shihezi	Upper	200–340		Yellowish green, purplish gray, blue gray sandy mudstone intercalated with grayish green, yellowish green arkose, and manganese concretions are observed in the layers
							Light grayish green and yellowish green pebbly middle coarse sandstone intercalated with grayish green and yellowish green bauxitic mudstone
		Lower		Lower	80–200		Yellowish green thick pebbly middle-coarse sandstone
			Shanxi		37–125		Mudstone mixed with sandstone and coal seam
	Carboniferous		Taiyuan		22–276		
			Benxi		15–58		
Lower Paleozoic	Ordovician	Lower	Majiagou		100–1000		Gray thick limestone and off-white dolomite mixed with mud-banded limestone

Figure 1: Lithologic and stratigraphic sequence of the Ordos Basin, illustrating the positions and geological characteristics of the main injection formations (modified from Li et al. [29]).

geochemical transport simulator [18] used in this study. The multiphase flow, heat flow, and chemical transport are governed by the principle of mass (energy) conservation. The general conservation equation can be written as follows:

$$\frac{\partial M_\kappa}{\partial t} = -\nabla F_\kappa + q_\kappa, \quad (1)$$

where the subscript κ is the mass component or heat component, M_κ is the mass or energy of component κ, t is the time, F_κ denotes the mass or heat flux, and q_κ is the sources or sinks. The calculation here contains the component in all phases.

After space and time discretization, the governed equations for fluid flow are transformed to a set of coupled nonlinear algebraic equations and can be solved by Newton-Raphson iteration methods [18]. The thermodynamic variables such as fluid velocities and phase saturations are obtained and used for chemical transport simulation.

Table 1: Mineral composition of formations [25–27] and possible secondary minerals used in the simulations.

Minerals of formations	Mineral modelled	Chemical composition	Volume fraction (vol.%)		
			Liujiagou	Shiqianfeng	Shihezi
		Primary minerals			
Quartz	Quartz	SiO_2	27	65	66
Alkali-feldspar	K-feldspar	$KAlSi_3O_8$	14	9	0
Plagioclase	Oligoclase	$Ca_{0.2}Na_{0.8}Al_{1.2}Si_{2.8}O_8$	24	16	6
Illite	Illite	$K_{0.6}Mg_{0.25}Al_{1.8}(Al_{0.5}Si_{3.5}O_{10})(OH)_2$	17	4.5	18.5
Kaolinite	Kaolinite	$Al_2Si_2O_5(OH)_4$	6	0	0
Chlorite	Chlorite	$Mg_{2.5}Fe_{2.5}Al_2Si_3O_{10}(OH)_8$	8.5	0	0
Smectite	Smectite-Na	$Na_{0.290}Mg_{0.26}Al_{1.77}Si_{3.97}O_{10}(OH)_2$	1.75	1.25	1.75
	Smectite-Ca	$Ca_{0.145}Mg_{0.26}Al_{1.77}Si_{3.97}O_{10}(OH)_2$	1.75	1.25	1.75
Calcite	Calcite	$CaCO_3$	0	3	3
Dolomite	Dolomite	$CaMg(CO_3)_2$	0	0	3
		Secondary minerals			
	Magnesite	$MgCO_3$			
	Albite	$NaAlSi_3O_8$			
	Siderite	$FeCO_3$			
	Ankerite	$CaMg_{0.3}Fe_{0.7}(CO_3)_2$			
	Dawsonite	$NaAlCO_3(OH)_2$			
	Hematite	Fe_2O_3			
	Halite	NaCl			
	Anhydrite	$CaSO_4$			

Table 2: Aqueous concentrations of in situ water [26, 27, 32] and initial aqueous concentrations for simulations.

Components	Liujiagou		Shiqianfeng		Shihezi	
	(mg/L)	(mol/kg H_2O)	(mg/L)	(mol/kg H_2O)	(mg/L)	(mol/kg H_2O)
Na^+	7816	1.09	4560	4.19×10^{-1}	2356	1.97×10^{-1}
Ca^{2+}	14511.02	1.32×10^{-2}	6450	5.66×10^{-2}	1067.33	2.70×10^{-5}
Mg^{2+}	894.6	7.09×10^{-7}	198.72	5.59×10^{-13}	4.47	2.25×10^{-5}
K^+	34.15	6.84×10^{-5}	24.453	1.82×10^{-3}	76.42	2.87×10^{-5}
Fe^{2+}	2.24	1.02×10^{-4}	19.04	1.25×10^{-5}	27.47	9.52×10^{-11}
Cl^-	39739.84	1.12	17940	5.06×10^{-1}	5339.34	1.50×10^{-1}
SO_4^{2-}	2075.01	3.93×10^{-4}	1940	1.85×10^{-2}	46.28	2.26×10^{-7}
HCO_3^-	25.22	1.77×10^{-3}	56.852	6.50×10^{-4}	520.26	4.57×10^{-2}
AlO_2^-	0.1845	1.32×10^{-8}	0.00324	2.77×10^{-8}	0.0057	7.59×10^{-8}
SiO_2(aq)	1.18	5.15×10^{-4}	708	5.89×10^{-4}	19.5	6.63×10^{-4}
pH		7.03		6.68		7.92
Temperature		55°C		62°C		67°C

Note. Data under mg/L are aqueous concentrations of in situ water; data under mol/kg H_2O are the initial aqueous concentrations for simulations.

To reproduce a geochemical system, the concentrations of aqueous complexes composed of basis species are expressed as

$$c_i = K_i^{-1}\gamma_i^{-1}\prod_j^{N_c} c_j^{v_{ij}}\gamma_j^{v_{ij}}, \quad (2)$$

where c is the molal concentration of aqueous components, γ is the thermodynamic activity coefficient, K is the equilibrium constant, subscripts i and j mean the index of the aqueous complexes and basis species, respectively, the subscript i also means the ith reaction to composing the ith aqueous complexes, v_{ij} is the stoichiometric coefficient of jth basis species in the ith reaction, and N_c is the total number of basis species.

For the dissolution and precipitation of equilibrium minerals, the mineral saturation ratio is expressed as

$$\Omega_m = K_m^{-1}\prod_{j=1}^{N_c} c_j^{v_{mj}}\gamma_j^{v_{mj}}, \quad (3)$$

where subscript m is the equilibrium mineral index and K_m is the corresponding equilibrium constant. Meanwhile the

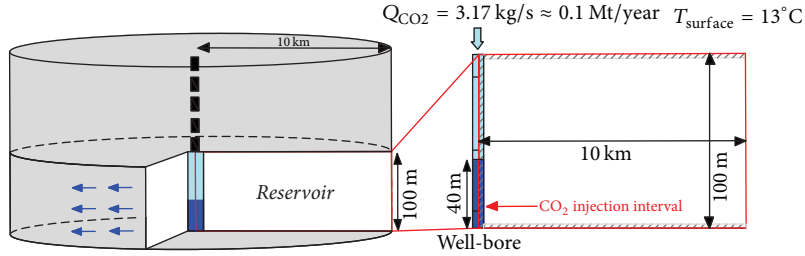

Figure 2: Schematic representation of the 2D radial model.

dissolution and precipitation of kinetic minerals are modelled with a rate expression given by Lasaga et al. [34]:

$$r_n = \pm k_n A_n \left|1 - \Omega_n^{\theta}\right|^{\eta}, \quad (4)$$

where k is the rate constant, A is the specific reactive surface area, Ω is the kinetic mineral saturation ratio which is defined as (3), subscript n is the kinetic mineral index, and parameters θ and η are determined from experiment or taken as equal to one.

Reactions involving aqueous and gaseous phases are assumed to be at equilibrium and the governing equation according to the Mass-Action Law is as follows:

$$p_f \Gamma_f K_f = \prod_{j=1}^{Nc} c_j^{v_{fj}} \gamma_j^{v_{fj}}, \quad (5)$$

where p is the partial pressure of gas and Γ is the gas fugacity coefficient.

Porosity changes of the medium are directly calculated from the volume changes as a result of mineral precipitation and dissolution [18]. The calculation of permeability changes in TOUGHREACT depends on the medium type.

3.2. Model Setup and Simulation Parameters. In this study, we focus on the long-term CO_2-water-rock interactions in reservoir; therefore we simplify the three formations as homogeneous sandstones. A two-dimensional (2D) radial model is applied with thickness of 100 m and an external radius of 10 km (Figure 2). The model contains 10 layers in the vertical direction, and it is divided into 101 radial grid elements logarithmically increasing from the injection well in the radial direction. The injection well is modelled as a circular grid element of $R = 0.2$ m, while the outermost grid is specified with a large volume of 10^{50} m^3 representing an infinite lateral boundary. The top and bottom boundaries of the model are regarded as impermeable layers. Similar models have been used in previous studies [8, 31, 33]. The injection interval is 40 m thick at the bottom of the injection well. CO_2 is injected into the formation at a constant rate of 3.17 kg/s for three years. The fluid flow and geochemical transport simulation are running for 10,000 years, which is a reasonable time scale for CO_2 long-term sequestration [15, 33, 35, 36].

The hydrogeological and petrophysical parameters are based on the actual underground conditions. The initial pressures of the Liujiagou, Shiqianfeng, and Shihezi formations are 16 MPa, 18.9 MPa, and 21 MPa, respectively, while the temperatures are 55°C, 62°C, and 67°C, respectively. The initial mineral compositions and aqueous concentrations are presented in Section 2. The initial porosities of the Liujiagou, Shiqianfeng, and Shihezi formations used in the simulations are 10%, 12.9%, and 12.6%, while the permeabilities are 2.81×10^{-15} m^2, 6.58×10^{-15} m^2, and 5.99×10^{-15} m^2, respectively. Alkali-feldspar and plagioclase are modelled as K-feldspar and oligoclase, and smectite is regarded as a combination of 50% smectite-Na and smectite-Ca referring to previous studies [16, 17]. Capillary pressure and relative permeability are calculated from the models of van Genuchten [37] and Corey [38]. The details are given in Table 3. Other parameters are taken from Xu et al. [31].

4. Results and Discussion

4.1. Time Evolution of CO_2 Trapping Mechanisms. Injected CO_2 can be directly trapped as free-gas (supercritical fluid) by low-permeability caprocks and then dissolves into groundwater and reacts with rock minerals leading to precipitation of carbonates [16]. The whole process can be classified as three trapping mechanisms: free-gas trapping, solubility trapping, and mineral trapping. Using TOUGHREACT as the simulator, the abundance of CO_2 trapped in different mechanisms can be calculated from

$$M_{CO2}^{g} = \sum_{n=1} \left(V_n \phi_n \mathrm{Sg}_n \mathrm{Dg}_n\right) \quad (6)$$

$$M_{CO2}^{l} = \sum_{n=1} \left(V_n \phi_n \mathrm{Sl}_n \mathrm{Dl}_n X_{CO2}\right) \quad (7)$$

$$M_{CO2}^{s} = \sum_{n=1} \left(V_n \left(1 - \phi_n\right) \mathrm{SM}_{CO2}\right), \quad (8)$$

where the superscripts g, l, and s indicate CO_2 trapped as free-gas, aqueous phase, and minerals, respectively, M_{CO2} is the CO_2 trapping capacity, the subscript n is the index of grid blocks, V is the volume, ϕ is the porosity, Sg and Sl are the gas saturation and liquid saturation, Dg and Dl are the density of gas and liquid phase, X_{CO2} is the mass fraction of CO_2 in aqueous phase, and SM_{CO2} is CO_2 mineral trapping capacity per unit volume medium.

The evolution of CO_2 trapping mechanisms of the three formations over time is shown in Figures 3(a), 3(b), and 3(c). During the injection period (the first three years), the CO_2 trapping mechanisms in the three formations are similar.

Table 3: Hydrogeological parameters of the three formations used in this study.

Parameters	Liujiagou formation	Shiqianfeng formation	Shihezi formation
Permeability (m^2)	2.81×10^{-15}	6.58×10^{-15}	5.99×10^{-15}
Porosity	0.100	0.129	0.126
Pore compressibility (Pa^{-1})	4.5×10^{-10}	4.5×10^{-10}	4.5×10^{-10}
Rock grain density (kg/m^3)	2600	2600	2600
Temperature (°C)	55	62	67
Pressure (MPa)	16	18.9	21
Salinity (wt.%)	6	3	0.9
Residual gas saturation, S_{gr}	0.05	0.05	0.05
Residual liquid saturation, S_{lr}	0.3	0.3	0.3
van Genuchten, P_0 (kPa)	19.61	19.61	19.61
van Genuchten, λ (1/Pa)	0.457	0.457	0.457

The CO_2 free-gas trapping and CO_2 solubility trapping keep growing, while the CO_2 mineral trapping remains inactive. At the end of injection period, 80% of injected CO_2 remains as free-gas in each formation. Then the CO_2 free-gas trapping decreases, while the CO_2 solubility trapping continues rising up. The CO_2 mineral trapping in the three formations starts at the 100 years and the final CO_2 mineral trapping capacity is almost the same (nearly all the CO_2 gases are trapped in minerals at 10,000 years).

Standard deviation is usually used to quantify the dispersion degree of a set of data [39]. In this study, there are three CO_2 amounts for the three formations under each CO_2 trapping mechanism. They are regarded as a set of data, the standard deviation of which is calculated to quantify the difference among the three CO_2 amounts. As shown in Figure 3(d), each line denotes one trapping mechanism. The standard deviations of the three trapping mechanisms increase greatly from 100 years, which corresponds to the beginning of CO_2 mineral trapping. After that then the difference of mineral trapping capacities becomes the largest. The different CO_2 mineral trapping capacities affect the CO_2 amounts of the other two trapping mechanisms. Thus the standard deviation peaks of the three trapping mechanisms occur at about 1000–2000 years. It can be concluded that the evolution of CO_2 trapping mechanisms is dominated by the CO_2-water-rock interactions in a large time scale (more than 1000 years). CO_2-water-rock interactions should be the key factor for the evaluation of long-term CO_2 geological storage.

To assess the CO_2 mineral trapping capability of the three formations, we calculate the abundance of CO_2 sequestrated in minerals (Figure 4) using

$$M_{\mathrm{CO_2min}_a} = \sum_{n=1}^{n_{\max}} \left(V_n \left(1 - \phi_n\right) V_a W_{\mathrm{CO_2min}_a} \rho_{\mathrm{rock}} \right), \quad (9)$$

where the superscript a means the CO_2 trapping mineral, ρ_{rock} is the density of the host rock 2600 kg/m^3, and $W_{\mathrm{CO_2min}_a}$ is the molecular weight percent of CO_2 in mineral a.

CO_2 is injected into the formation at the constant rate of 3.17 kg/s (100,000 tons/year) for three years, and thus the total amount of injected CO_2 in each formation is 3×10^8 kg. At the end of simulation, the CO_2 mineral trapping capacities of the Liujiagou, Shiqianfeng, and Shihezi formations are 2.99×10^8 kg, 2.85×10^8 kg, and 2.79×10^8 kg, respectively. In the Liujiagou formation, the amounts of CO_2 immobilized in calcite, dawsonite, and siderite are 2.07×10^8 kg, 4.61×10^7 kg, and 4.59×10^7 kg, respectively. In the Shiqianfeng formation, the amounts of CO_2 immobilized in calcite and dawsonite are 1.84×10^8 kg and 1.01×10^8 kg. In the Shihezi formation, the amounts of CO_2 immobilized in calcite, dawsonite, and magnesite are 1.49×10^8 kg, 1.42×10^7 kg, and 1.16×10^8 kg, respectively (Figure 4). It can be inferred that calcite is a common CO_2 trapping mineral, while dawsonite, siderite, and magnesite precipitation depend on specific formation conditions.

4.2. pH Changes. CO_2 dissolution induces a series of acidic reactions, lowering the pH of the formation water. Figure 5 shows the pH spatial distribution of the Liujiagou formation at different times, which is similar to the cases of the Shiqianfeng and Shihezi formations (not shown). Figure 5 also infers the spatial distribution of CO_2 plume. We select points A, B, and C to represent CO_2-rich zone and near-well and far-well zone and take point C as a reference point.

As shown in Figure 6, pH at points A and B falls sharply during the injection period (the first three years) and increases distinctly after hundreds of years. The changes of pH at point A lag behind point B because point B is beneath point A, which is closer to the injection interval. It can be concluded that the decrease in pH is caused by CO_2 dissolution (Reaction 1 in Table 4), while the increase in pH is resulting from mineral dissolution (Reaction 2–5 in Table 4).

We take the pH at different times as a set of data and calculate the standard deviations to show the different buffering degrees in the three formations. For the Liujiagou, Shiqianfeng, and Shihezi formations, the buffering degrees are quantified as 1.447, 0.977, and 0.318 at point A and 1.814, 1.376, and 1.160 at point B, respectively. Hence, the descending order of the amounts of dissolved minerals for the three formations is as follows: the Liujiagou formation, the Shiqianfeng formation, and the Shihezi formation.

4.3. Mineral Dissolution. Point C is regarded as a reference point in far-well zone, mineral dissolution and precipitation

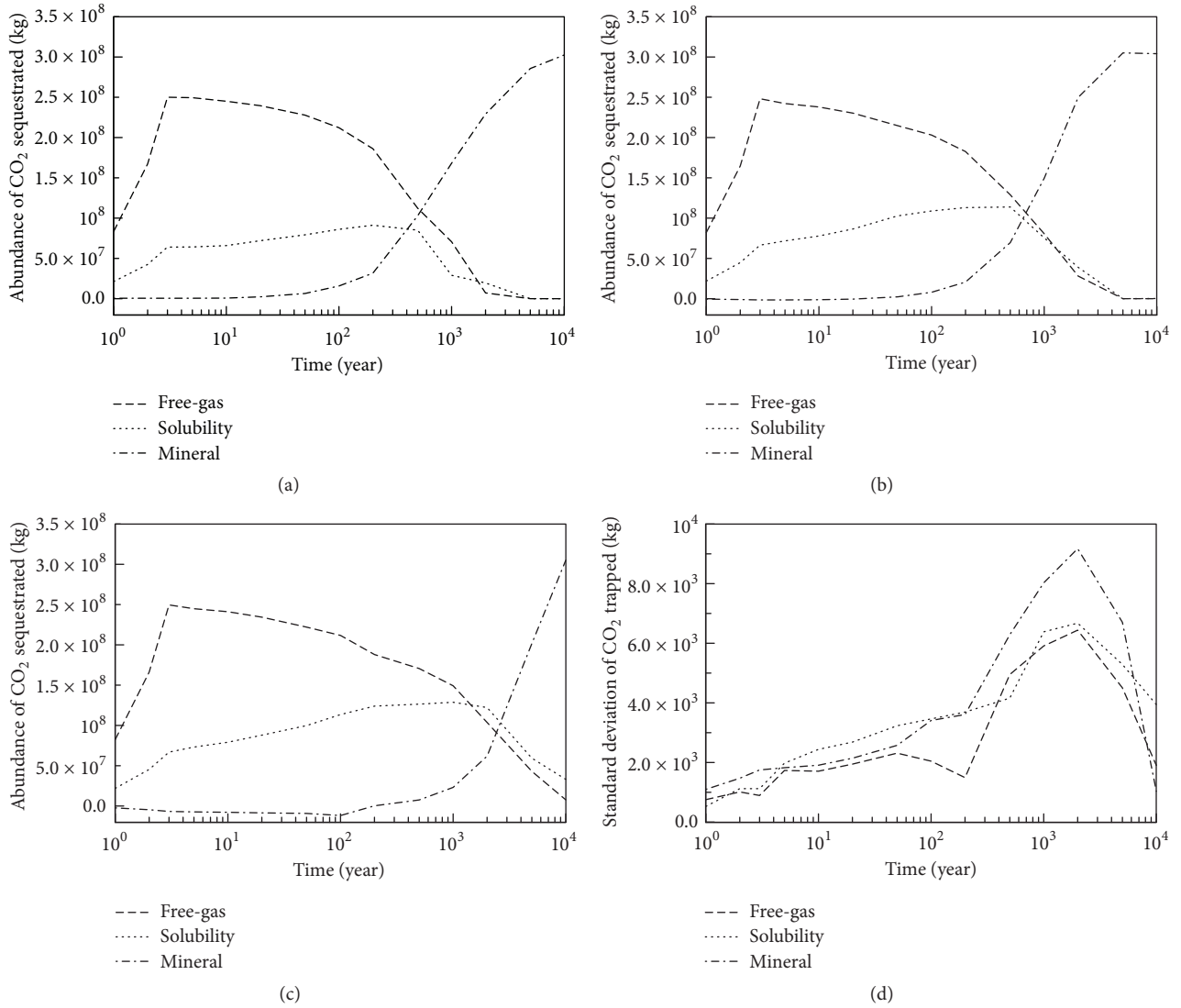

Figure 3: The evolution of the injected CO_2 in different trapping mechanisms for the Liujiagou formation (a), the Shiqianfeng formation (b), and the Shihezi formation (c) and the evolution of standard deviations for different trapping mechanisms (d) over time.

of which are not affected by CO_2-water-rock interactions. Then we deduct the changes in mineral and ion of point C from points A and B to analyze the geochemical reactions induced by CO_2 injection (Figures 7, 8, and 9). Figure 7 shows the mineral dissolution induced by CO_2-water-rock interactions in the three formations, which is consistent with the quantified pH buffering degrees in Section 4.2.

Oligoclase, smectite-Ca, and illite are common initial minerals in the three formations. As shown in Figure 7, oligoclase dissolves steadily and supplies Ca^{2+} and Mg^{2+}. The amounts of dissolved oligoclase at point A are very close to that at point B. However, more dissolved oligoclase occurs in the Liujiagou and Shiqianfeng formations due to the higher initial oligoclase abundance. Smectite-Ca firstly precipitates with sufficient Ca^{2+} and Mg^{2+} in the first 5000 years. Then it dissolves to provide Ca^{2+} and Mg^{2+}, which are needed for precipitation of other minerals. Illite only dissolves at point A in the Liujiagou and Shiqianfeng formations that can release Mg^{2+} and K^+. K-feldspar is an initial mineral in both the Liujiagou and Shiqianfeng formations, while it only dissolves at point B of these formations and supplies K^+ (Figures 7(b) and 7(d)). Chlorite only dissolves in the Liujiagou formation as an initial mineral, releasing Mg^{2+} and Fe^{2+} (Figures 7(a) and 7(b)). In addition, as albite is a selected secondary mineral in the three formations, the decrease in volume fraction of albite (Figures 7(e) and 7(f)) is due to the greater precipitation of albite at point C than at points A and B, which suggests CO_2 is unfavorable for albite precipitation.

It can be inferred that oligoclase and smectite-Ca are Ca^{2+} sources in the three formations. Mg^{2+} is supplied by smectite-Ca, illite, and chlorite in the Liujiagou formation, smectite-Ca and illite in the Shiqianfeng formation, and smectite-Ca in the Shihezi formation. K^+ in the Liujiagou and Shiqianfeng formations is provided by illite and K-feldspar

Table 4: The main dissolution reactions in this study.

Reaction 1: dissolution of CO_2:
$CO_2(gas) \leftrightarrow CO_2(aq)$; $CO_2(aq) + H_2O \leftrightarrow H_2CO_3$; $H_2CO_3 \leftrightarrow H^+ + HCO_3^-$; $HCO_3^- \leftrightarrow H^+ + CO_3^{2-}$
Reaction 2: dissolution of chlorite:
$Mg_{2.5}Fe_{2.5}Al_2Si_3O_{10}(OH)_8 + 10H^+ \leftrightarrow 2.5Mg^{2+} + 2.5Fe^{2+} + Al_2Si_2O_5(OH)_4 + Si(OH)_4 + 5H_2O$
Reaction 3: dissolution of oligoclase:
$CaNa_4Al_6Si_{14}O_{40} + 6H^+ + 19H_2O \leftrightarrow Ca^{2+} + 4Na^+ + 3Al_2Si_2O_5(OH)_4 + 8Si(OH)_4$
Reaction 4: dissolution of illite:
$K_{0.6}Mg_{2.5}Al_{1.8}(Al_{0.5}Si_{3.5}O_{10})(OH)_2 + 5.6H^+ + 1.8H_2O \leftrightarrow 2.5Mg^{2+} + 0.6\,K^+ + 1.15Al_2Si_2O_5(OH)_4 + 1.2Si(OH)_4$
Reaction 5: dissolution of albite
$2Na(AlSi_3)O_8 + 2H^+ + 9H_2O \leftrightarrow 2Na^+ + Al_2SiO_5(OH)_4 + 4H_4SiO_4$

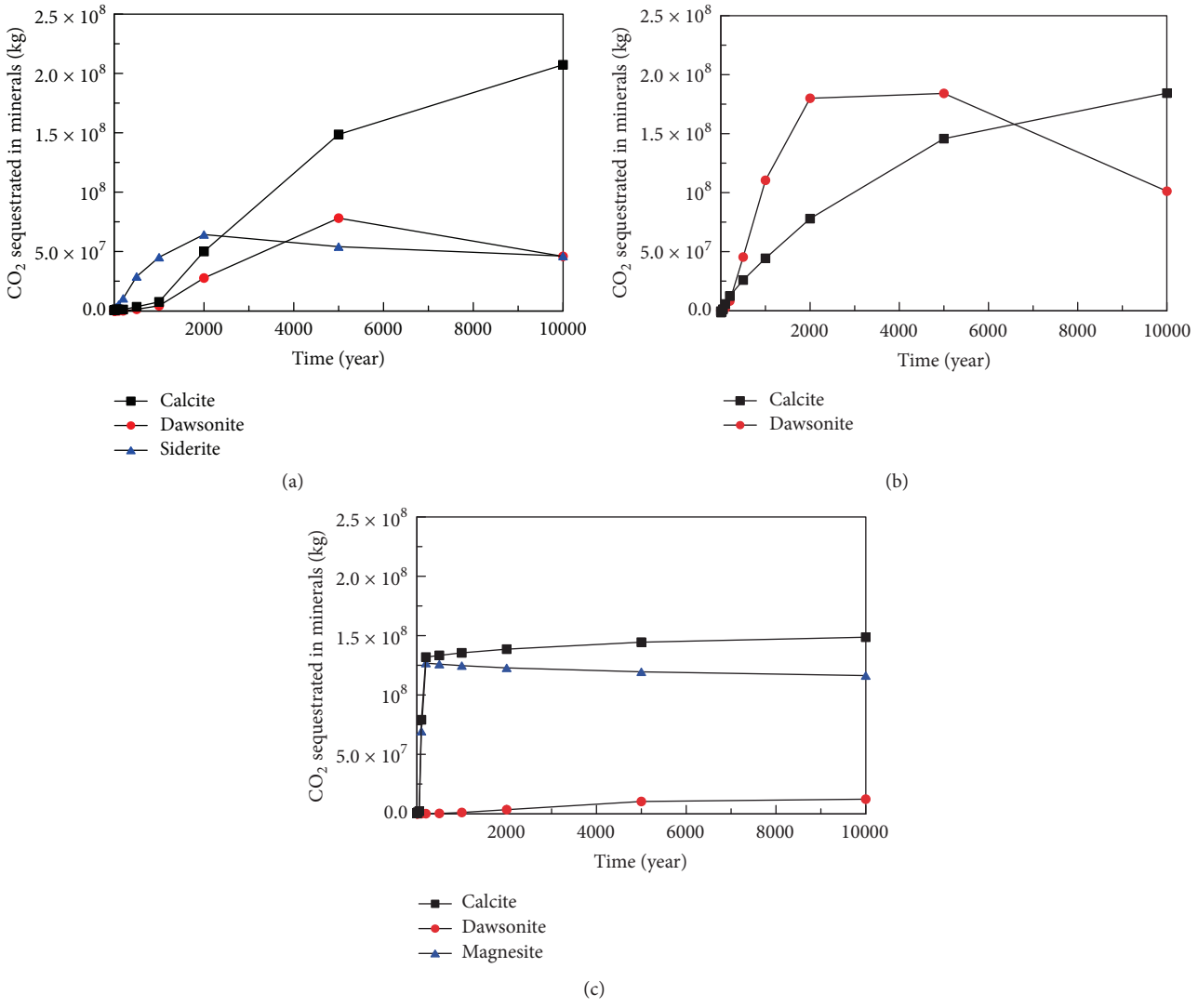

Figure 4: The amounts of CO_2 sequestrated in minerals for the Liujiagou formation (a), Shiqianfeng formation (b), and Shihezi formation (c) at different times.

dissolution, respectively. Fe^{2+} is only provided by chlorite in the Liujiagou formation. Na^+ is sourced from oligoclase in the three formations.

Figure 8 shows the changes in aqueous concentrations induced by CO_2-water-rock interactions. As mentioned above, mineral dissolution might increase the concentrations of Na^+, Fe^{2+}, Mg^{2+}, Ca^{2+}, and K^+ in the formation water. However, the concentration changes of K^+ and Fe^{2+} in the three formations remain zero (Figure 8). The changes of Mg^{2+} in the Liujiagou and Shihezi formations remain zero after 400

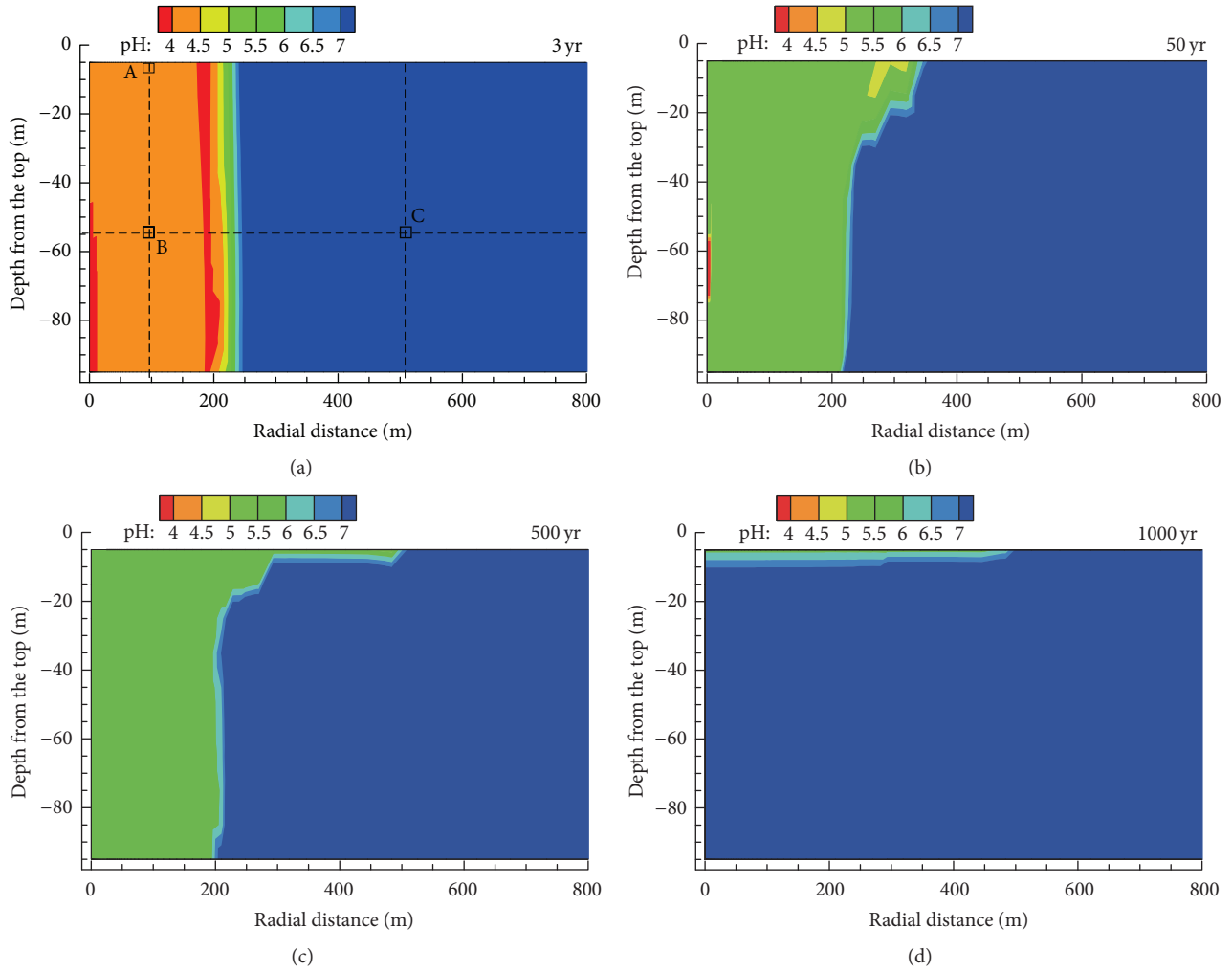

Figure 5: The pH spatial distribution of the Liujiagou formation at different times.

years and 200 years, respectively. The maximum reduction of Ca^{2+} occurs in the Liujiagou formation and the minimum in the Shihezi formation (Figures 8(a), 8(b), 8(e), and 8(f)). The concentration of Na^{+} in the Liujiagou and Shiqianfeng formations decreases in the first 30 years and then increases with a different extent (Figures 8(a), 8(b), 8(c), and 8(d)). For Shihezi formation, Na^{+} increases after 100 years (Figures 8(e) and 8(f)). It can be inferred that the aqueous concentration changes are affected not only by mineral dissolution but also by mineral precipitation. Then we investigate the mineral precipitation combined with aqueous concentrations changes in Section 4.4.

4.4. Mineral Precipitation. In the Liujiagou formation (Figures 7–9(a-b)), illite and K-feldspar are initial minerals. It can be inferred from the changes in the concentration of K^{+} (Figures 8(a) and 8(b)) that K-feldspar precipitation at point A is due to illite dissolution, while precipitation of illite at point B results from K-feldspar dissolution. Similarly, ankerite and siderite precipitate with chlorite dissolution providing Fe^{2+}. More chlorite dissolves at point A compared to point B due to lower pH, leading to more ankerite and siderite precipitation at point A. Precipitation of ankerite also needs Ca^{2+} and Mg^{2+}, which suggest that more Ca^{2+} and Mg^{2+} are provided at point A compared to point B.

For the Liujiagou formation (Figures 7–9(a-b)), Ca^{2+} is released by oligoclase dissolution constantly, which is used for precipitation of smectite-Ca, calcite, and ankerite in the first 5000 years. During this period, Ca^{2+} provided by oligoclase dissolution and consumed by smectite-Ca precipitation at point A is close to that at point B (Figure 8(a, b) and Figure 9(a, b)). Hence the minor precipitation of calcite at point A left more Ca^{2+} for precipitation of ankerite than point B. In addition, smectite-Ca and ankerite all disappear at the end of simulation so that the final calcite abundances at points A and B are consistent.

The concentration of Mg^{2+} in the Liujiagou formation firstly increases due to chlorite dissolution. Then smectite-Ca and illite dissolution also provide Mg^{2+} at point A. Meanwhile, Mg^{2+} at point B is released by minor dissolution of smectite-Ca and chlorite and consumed by illite precipitation. Hence, there is more Mg^{2+} at point A for precipitation of

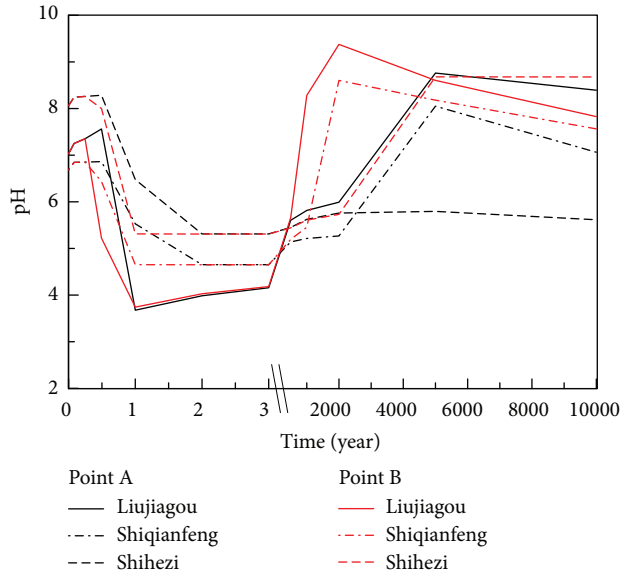

FIGURE 6: The evolution of pH at point A and point B for the Liujiagou, Shiqianfeng, and Shihezi formations over time.

ankerite. Na^+ released by oligoclase dissolution at point A is close to that at point B. Then the larger increase in Na^+ at point A can be explained by additional albite dissolution and minor smectite-Na precipitation. Dawsonite precipitates at both points A and B with sufficient Na^+ and high CO_2 saturation. However, CO_2 moves upward by buoyance in the near-well zone (point B) so that dawsonite at point B disappears at the end of simulation.

In the Shiqianfeng formation (Figures 7–9(c-d)), illite and K-feldspar are also initial minerals. The changes in concentration of K^+ also remain zero. Therefore, all dissolved illite is transformed into K-feldspar at point A as the case in the Liujiagou formation. However, K-feldspar precipitation also occurs at point B due to illite dissolution providing K^+ in the first 5000 years, and after that then K-feldspar dissolves to supply K^+ for illite precipitation. It can be inferred that illite is transformed into K-feldspar with higher CO_2 saturation and lower pH (Figure 6) in the Liujiagou and Shiqianfeng formations, while it reverses with lower CO_2 saturation and higher pH. Besides, precipitation of ankerite and siderite does not occur without chlorite providing Fe^{2+}.

For Shiqianfeng formation (Figures 7–9 (c-d)), Ca^{2+} is also released by oligoclase and used for precipitation of smectite-Ca and calcite in the first 5000 years. Then smectite-Ca dissolves to provide more Ca^{2+} for calcite precipitation. At the end of simulation, the final calcite abundance at point A is consistent with that at point B. Mg^{2+} released by illite dissolution is used for precipitation of smectite-Ca and smectite-Na in the first 5000 years. Then smectite-Ca dissolves to supply Mg^{2+}, which is used for precipitation of smectite-Na at point A and precipitation of smectite-Na and illite at point B. Thus minor smectite-Na precipitation occurs at point B than point A. Na^+ released by oligoclase contributes to the precipitation of smectite-Na and dawsonite. There is more dawsonite precipitates in the Shiqianfeng formation than the Liujiagou formation, without ankerite and siderite immobilizing the injected CO_2. As a result, there are less Na^+ and minor smectite-Na precipitation in the Shiqianfeng formation.

In the Shihezi formation (Figures 7–9(e-f)), illite is an initial mineral, while K-feldspar is not (Table 1). Thus illite might be the only K^+ source. However, it does not dissolve to provide K^+ for K-feldspar precipitation at point A (Figure 7(e) and Figure 9(e)) with low pH and high CO_2 saturation (Figures 5 and 6), although 18.5% (volume fraction) of host rock is illite (Table 1). Also, there is no K^+ exchange between illite and K-feldspar at point B (Figures 7(f) and 9(f)). Ankerite and siderite does not precipitate because there is no chlorite (Table 1) supplying Fe^{2+}.

For Shihezi formation (Figures 7–9(e-f)), Ca^{2+} released by dolomite is consumed by precipitation of calcite in the first 50 years. Then calcite exchanges Ca^{2+} with dolomite in the next 150 years. However, calcite and dolomite are unstable due to low pH and high CO_2 saturation, and both of them disappear after 200 years. Then calcite precipitates again with pH increases due to dissolution of oligoclase and albite. Mg^{2+}, after an initial increase due to dolomite dissolution, is consumed by precipitation of smectite-Na and smectite-Ca. Na^+ released by oligoclase and albite is used for precipitation of smectite-Na and dawsonite. More dawsonite precipitates at point A compared to point B due to the higher CO_2 saturation at point A.

Mineral dissolution and precipitation induced by the injected CO_2 are analyzed by comparison of the three observation points (points A, B, and C) in the three formations. It can be inferred that quartz sandstones in the Shiqianfeng and Shihezi formations have lower pH buffering capacity. Illite and K-feldspar exchanged K^+ when they are both initial minerals. Chlorite is a key initial mineral providing Fe^{2+} for precipitation of ankerite and siderite. Calcite, dawsonite, and siderite are stable CO_2 trapping minerals, while ankerite, dolomite, and magnesite are not.

4.5. Distribution of Mineral Abundance. As described in Sections 4.2–4.4, the CO_2-water-rock interactions are mostly affected by variations in the initial mineral compositions. The mineral abundance changes at the end of simulation induced by CO_2-water-rock interactions are further analyzed in this part.

Figure 10 shows the mineral distribution of the three formations in the radial direction at the end of simulation at depths of −5 m and −55 m. According to pH changes and mineral alteration, the modelling system can be divided into three regions, which are CO_2 bearing zone, low gas saturation zone, and far-well zone. The initial mineral compositions of the three zones are the same. However, much more significant dissolution and precipitation of minerals occur in CO_2 bearing zone compared with far-well zone. Besides, CO_2 bearing zones at the end of simulation are also similar in shape to the CO_2 plume at the end of injection period (Figures 10 and 5), which indicates that the injected CO_2 barely moves after injection.

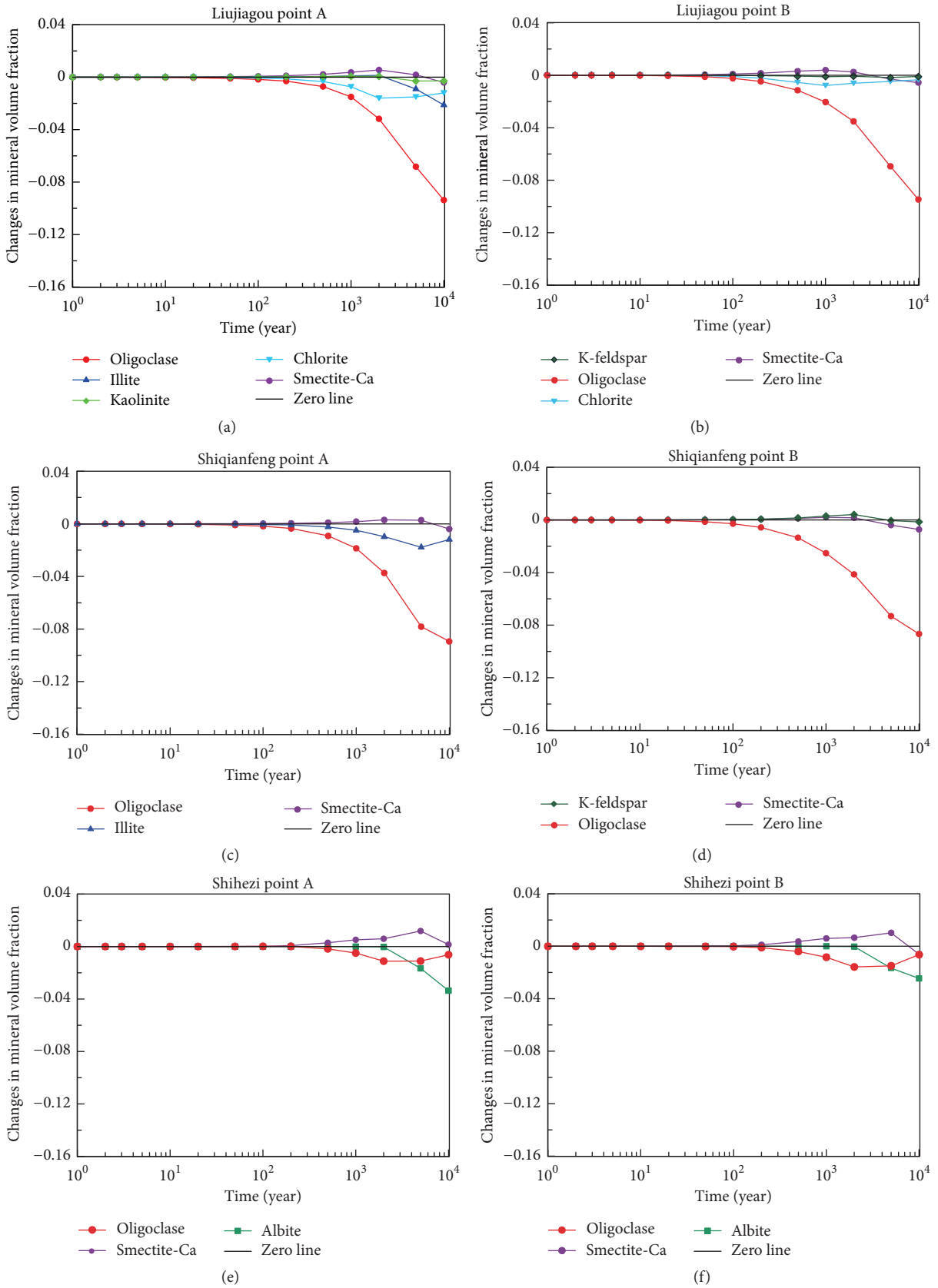

Figure 7: The evolution of dissolved minerals at points A and B for the Liujiagou formation (a, b), Shiqianfeng formation (c, d), and Shihezi formation (e, f) over time.

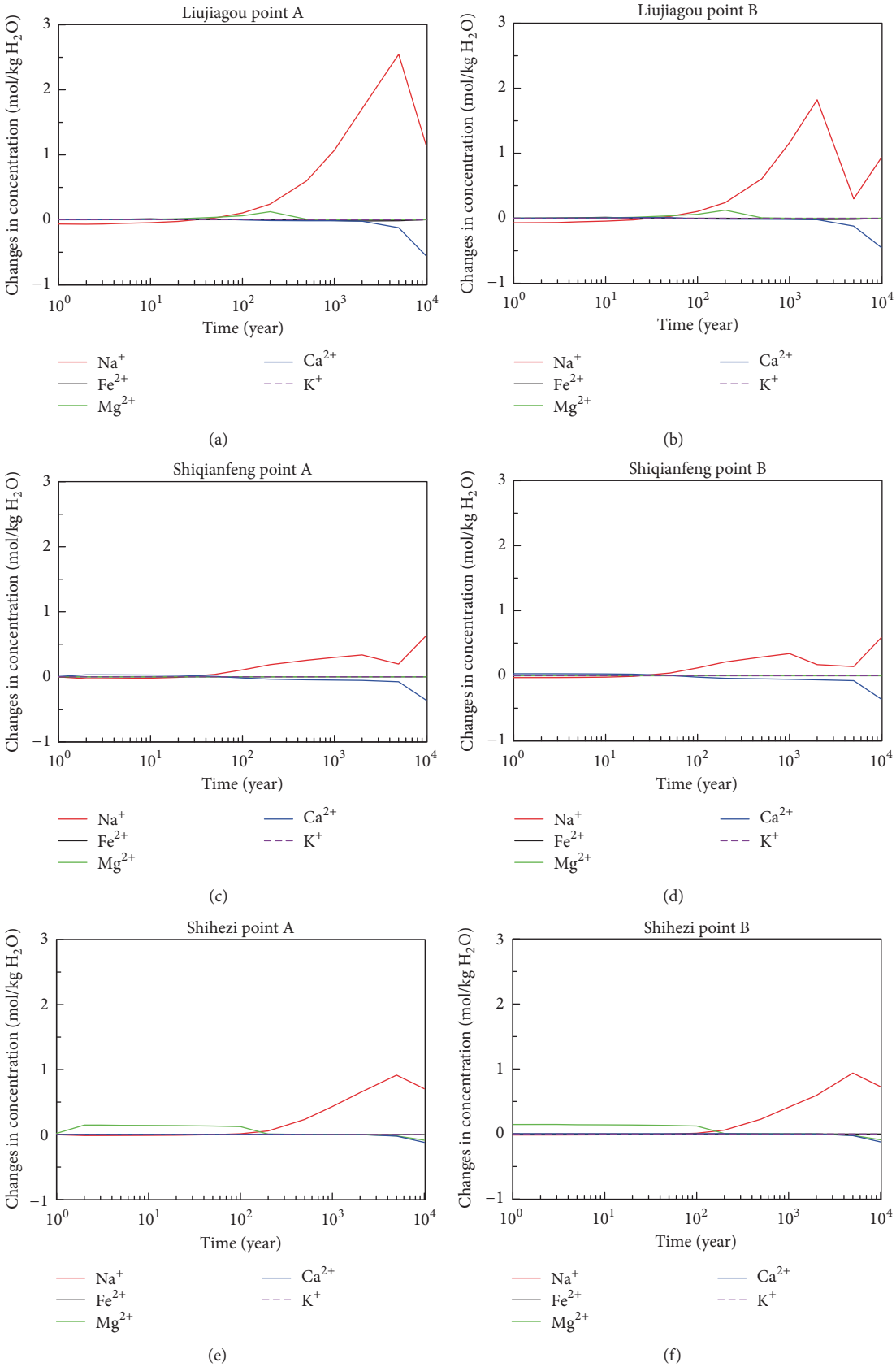

FIGURE 8: The evolution of changes in aqueous concentrations at points A and B for the Liujiagou formation (a, b), Shiqianfeng formation (c, d), and Shihezi formation (e, f) over time.

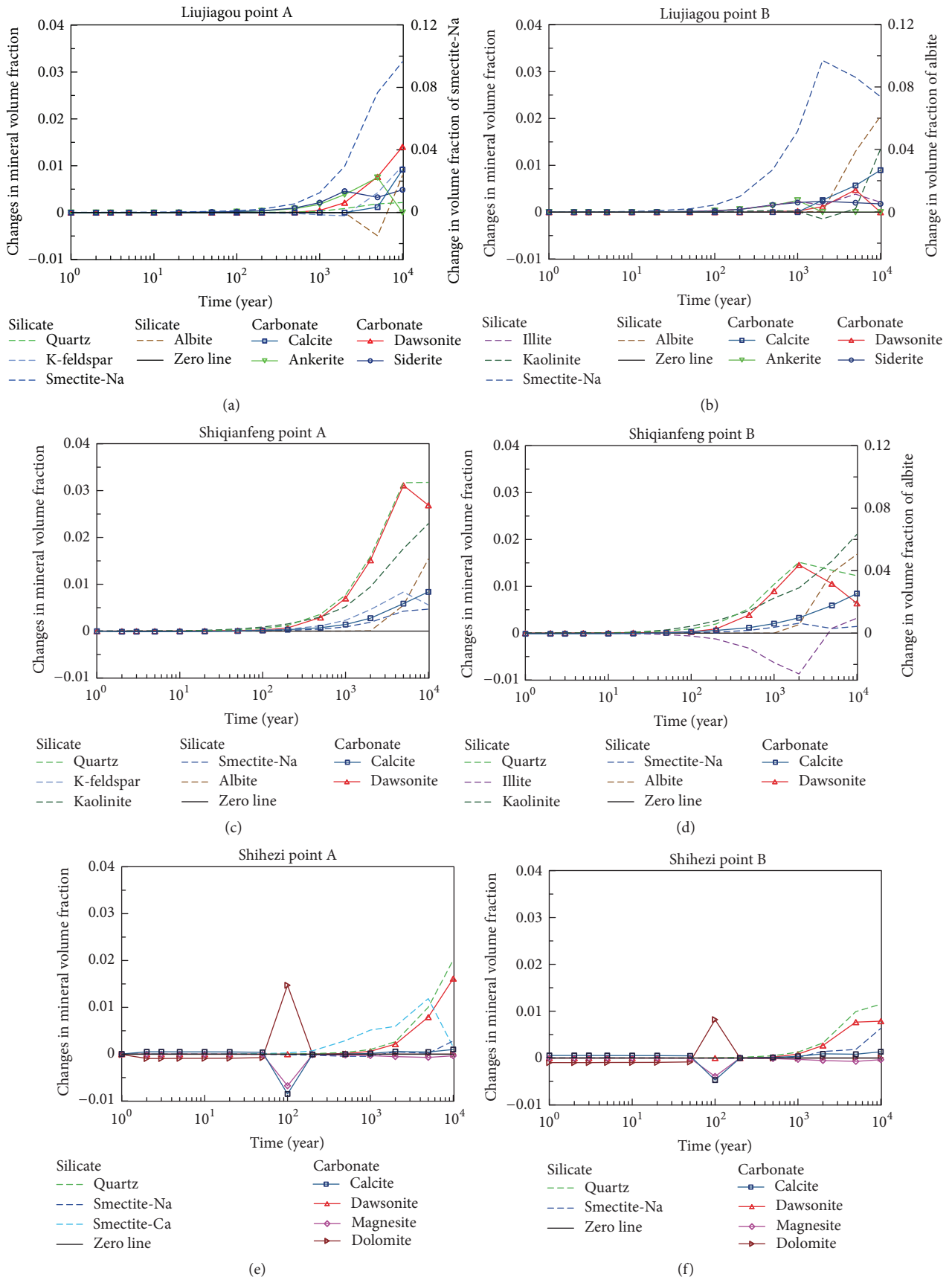

FIGURE 9: The evolution of mineral abundance changes at points A and B for the Liujiagou formation (a, b), Shiqianfeng formation (c, d), and Shihezi formation (e, f) over time.

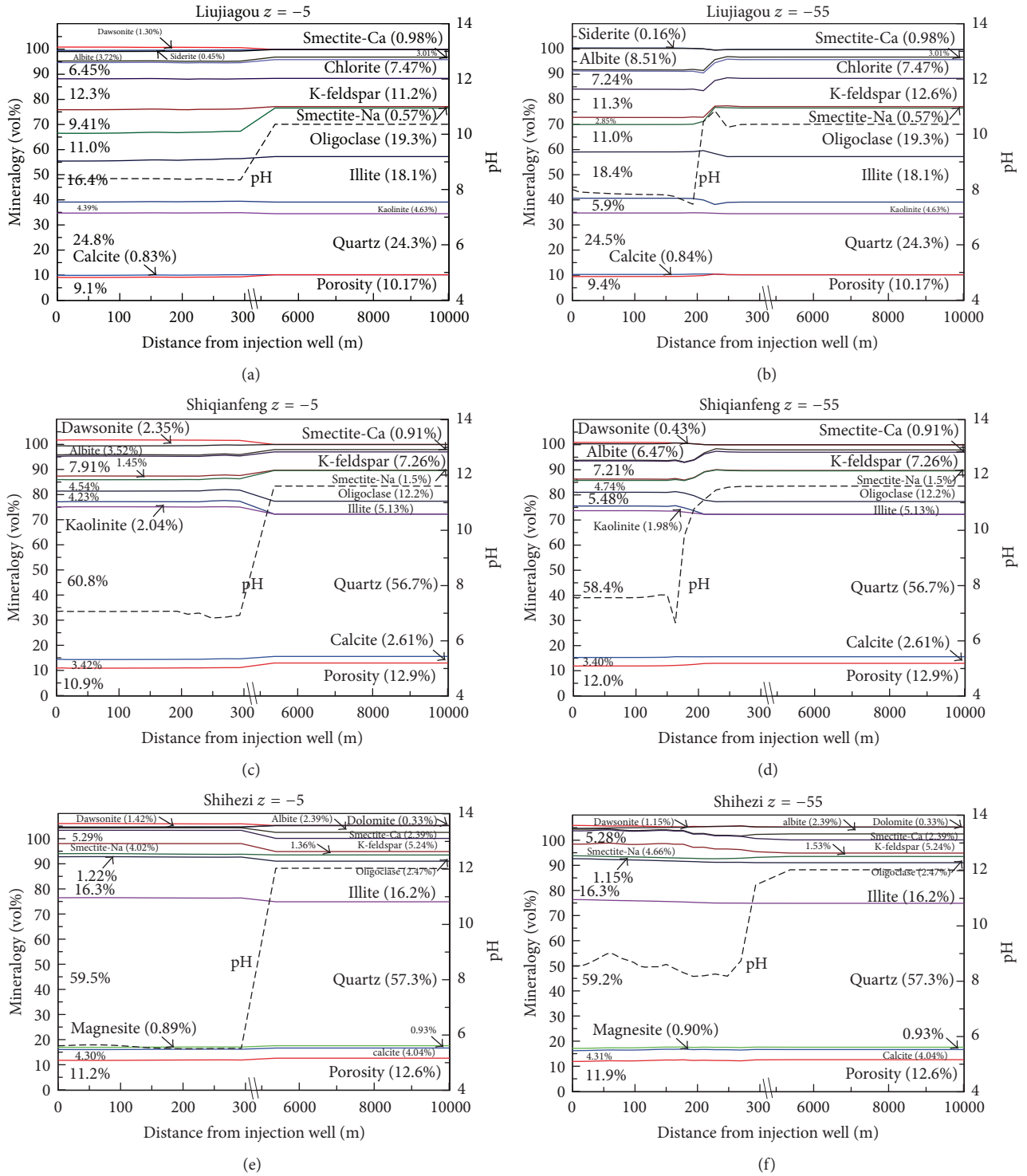

FIGURE 10: Mineral abundance of the Liujiagou formation (a, b), Shiqianfeng formation (c, d), and Shihezi formation (e, f) at the depths of −5 m and −55 m after 10,000 years.

To identify the mineral dissolution and precipitation induced by CO_2-water-rock interactions, we compare mineral abundances of CO_2 bearing zone with far-well zone (Table 5). For silicate minerals, quartz and smectite-Na precipitate and oligoclase and smectite-Ca dissolve impacted by CO_2-water-rock interactions in the three formations. For carbonate minerals, the CO_2 trapping mineral assemblages and abundances of the three formations are different, which can be seen in Table 5 for details.

4.6. Porosity and Permeability Changes. Porosity changes of the formation are directly calculated from the volume

Table 5: The changes in abundance of mineral dissolution and precipitation after 10,000 years.

Minerals modelled	Chemical composition	Mineral dissolution (↑) and precipitation (↓)					
		Liujiagou		Shiqianfeng		Shihezi	
		−5 m	−55 m	−5 m	−55 m	−5 m	−55 m
Primary minerals							
Quartz	SiO_2	↓	↓	↓	↓	↓	↓
K-feldspar	$KAlSi_3O_8$	↓	↑	↓	↑	↓	↓
Oligoclase	$Ca_{0.2}Na_{0.8}Al_{1.2}Si_{2.8}O_8$	↑	↑	↑	↑	↑	↑
Illite	$K_{0.6}Mg_{0.25}Al_{1.8}(Al_{0.5}Si_{3.5}O_{10})(OH)_2$	↑	↓	↑	↓	↓	↓
Kaolinite	$Al_2Si_2O_5(OH)_4$	↑	↓	↓	↓	/	/
Chlorite	$Mg_{2.5}Fe_{2.5}Al_2Si_3O_{10}(OH)_8$	↑	↑	/	/	/	/
Smectite-Na	$Na_{0.290}Mg_{0.26}Al_{1.77}Si_{3.97}O_{10}(OH)_2$	↓	↓	↓	↓	↓	↓
Smectite-Ca	$Ca_{0.145}Mg_{0.26}Al_{1.77}Si_{3.97}O_{10}(OH)_2$	↑	↑	↑	↑	↑	↑
Calcite	$CaCO_3$	↓0.83%	↓0.84%	↓0.81%	↓0.79%	↓1.68%	↓1.69%
Dolomite	$CaMg(CO_3)_2$	/	/	/	/	↑	↑
Secondary minerals							
Albite	$NaAlSi_3O_8$	↓	↓	↓	↓	↑	↑
Ankerite	$CaMg_{0.3}Fe_{0.7}(CO_3)_2$	/	/	/	/	/	/
Dawsonite	$NaAlCO_3(OH)_2$	↓1.30%	/	↓2.35%	↓0.43%	↓1.42%	↓1.15%
Siderite	$FeCO_3$	↓0.45%	↓0.16%	/	/	/	/
Magnesite	$MgCO_3$	/	/	/	/	↓0.04%	↓0.03%

Note. ↓ represents mineral precipitation; ↑ represents mineral dissolution; / represents nonexistent; data beside ↓ and ↑ is the volume fraction changes of minerals.

changes as a result of mineral precipitation and dissolution. As shown in Figure 11, porosity and permeability increase within the first 100 years and then decrease in the three formations. The maximum reduction of porosity and permeability occurs in the Shiqianfeng formation. It can be inferred that higher proportion of quartz in host rock is unfavorable for injectivity enhancing in large time scale.

The vertical distributions of porosity changes induced by CO_2-water-rock interactions at different times are shown in Figure 12. A column of model grids at a distance of 98.3 m from the injection well are selected to represent CO_2 bearing zone.

In the Liujiagou formation, porosity increases in the first 100 years and then decreases constantly. The larger decrease in porosity occurs at the top of the Liujiagou formation due to higher CO_2 saturation. However, the porosity at the top of the Liujiagou formation is greater than other parts at 5000 years due to ankerite dissolution. For the Shiqianfeng formation, porosity decreases with time. The increase in porosity in the first 100 years in Figure 11 is not shown in Figure 12, because single time points are used in Figure 12. The larger decrease in porosity at the top of the Shiqianfeng formation also occurs due to higher CO_2 saturation. But the greater porosity at the top of the Shiqianfeng formation occurs at 1000 years because of minor precipitation of quartz and kaolinite. In the Shihezi formation, porosity decreases after the initial increase within the first 100 years.

4.7. Comparisons with Previous Studies. Regarding the Shenhua CCS Project, the CO_2-water-rock interactions of major formations (the Liujiagou formation, the Shiqianfeng formation, and the Shihezi formation) have been studied by experimental methods [25–27], which shows good qualitative agreement with our studies.

For the Liujiagou formation, we conduct the modelling at a temperature of 55°C and a pressure of 16 MPa, while Tao [27] uses the temperatures of 60–100°C and the same pressure 16 MPa in the CO_2-water-rock interaction experiment. Dissolution of K-feldspar, oligoclase, and chlorite and precipitation of siderite within the experimental period of 1–25 days are observed. This is well consistent with our results in much longer simulation period. For the Shiqianfeng formation and the Shihezi formation, Wang [25] and Yang [26] conduct experiments at temperatures of 55–100°C and the same pressures of 18 MPa for 24 days. The minerals that dissolve and precipitate in the experiments agree with our simulations.

Besides, more minerals are dissolved rather than precipitated in the experiments, which may lead to the porosity increase. This shows good agreement with our results that porosity and permeability increase in the first 100 years, which is also consistent with the observed increasing injectivity at the Shenhua CCS demonstration project. However, we have also found the decreases in porosity and permeability after a long time of simulation (after 100 years). This might be because the experiment is limited by time scale so that we could not predict the long-term CO_2-water-rock interactions and related porosity changes.

We also compare our results with previous modelling studies [14, 16, 40, 41]. The decreases in the porosity and permeability of the three formations after 100 years agrees with the simulation results of Xu et al. [16] and Wang et al. [41]. We find that the CO_2 mineral trapping is affected by rock types of injected formations, especially the content of quartz.

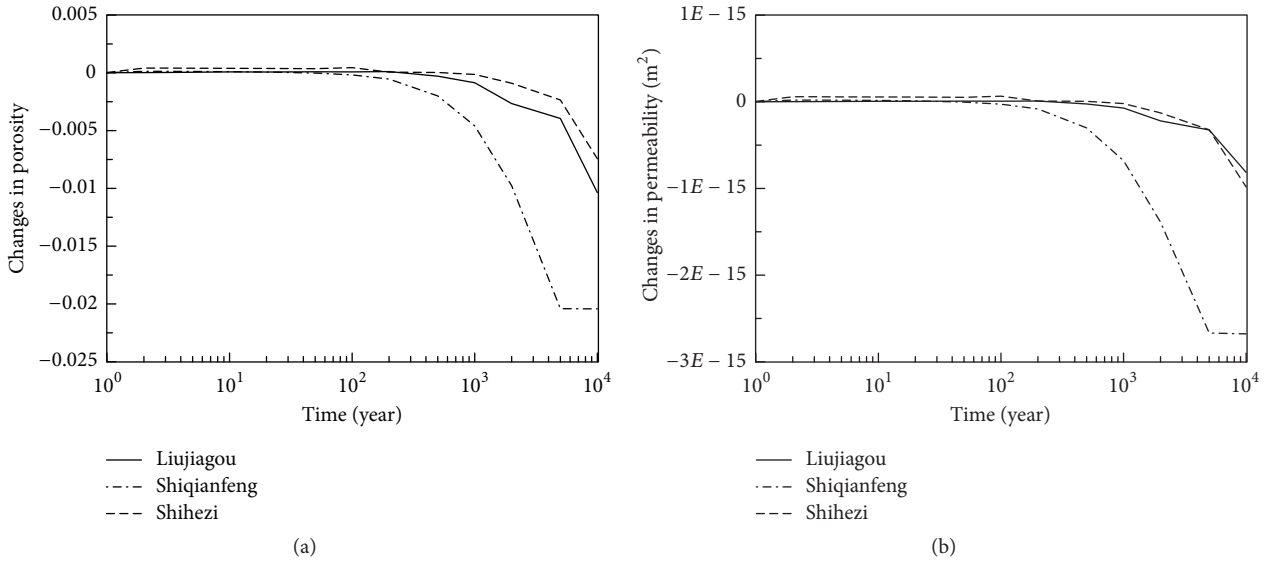

Figure 11: The evolution of changes in porosity (a) and permeability (b) at point A for the three formations over time.

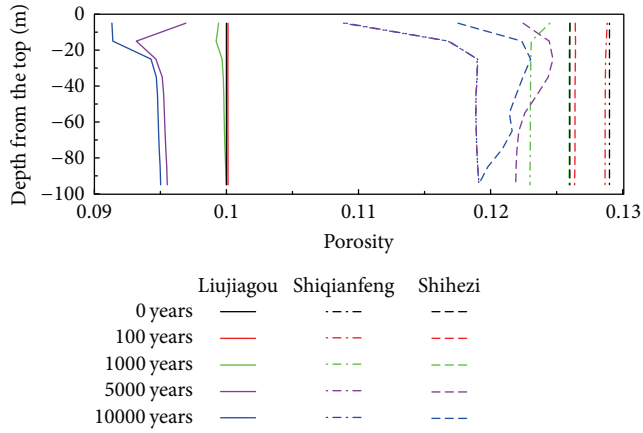

Figure 12: The vertical distributions of porosity changes in CO_2 bearing zone of the three formations at different times.

The volume fractions of quartz in the Shiqianfeng and Shihezi formations are 65% and 66%, respectively, which makes CO_2 mineral trapping capacities smaller than the Liujiagou formation. This is also demonstrated by Xu et al. [16] and Audigane et al. [14], and they found limited CO_2 sequestrated by mineral trapping due to the high quartz content in the formations.

It can be seen that K^+ exchanges between illite and K-feldspar when both of illite and K-feldspar are primary minerals in our study. However, this is different from Xu et al. [16] that they found illite and K-feldspar precipitation simultaneously. The differences can be explained by the fact that K^+ is only from illite and K-feldspar in Liujiagou and Shiqianfeng formations, while the dissolution of glauconite could provide K^+ for both illite and K-feldspar [16]. Chlorite as primary mineral provides Fe^{2+} and Mg^{2+} for precipitation of ankerite and siderite, which is consistent with Yang et al. [40] and Wang et al. [41]. The CO_2 trapping minerals are as follows: calcite, dawsonite, and siderite in the Liujiagou formation; calcite and dawsonite in the Shiqianfeng formation; calcite, dawsonite, and magnesite in the Shihezi formation. These trapping minerals are also observed in the above studies.

5. Conclusions

CO_2 geological storage in deep saline aquifers has great potential for reducing CO_2 emissions in China. The Shenhua CCS Project has finished its goal of injecting 100,000 tons/year CO_2 into the onshore saline aquifers of the Ordos Basin by the end of 2013. As the CO_2-water-rock interactions have great effect on the long-term CO_2 geological storage, geochemical modelling for the three injected formations of the Shenhua CCS Project is conducted for 10,000 years in this study. The results show the following.

(1) 80% injected CO_2 remains in the three formations as free-gas at the end of injection period. Then CO_2 plume beneath caprocks barely moves without injection pressure as driven force. The differences of CO_2 phase partition

among the three formations (as free-gas, aqueous phase, and minerals) increase greatly from 100 years and peak at 1000–2000 years. CO_2-water-rock interactions should be the key factor for the evaluation of long-term CO_2 geological storage.

(2) The CO_2 trapping mineral assemblages and abundances in the three formations are different. Total CO_2 mineral trapping capacities of the Liujiagou, Shiqianfeng, and Shihezi formations are 2.99×10^8 kg, 2.85×10^8 kg, and 2.79×10^8 kg, respectively, which suggests quartz sandstone formations have lower CO_2 mineral trapping capability. The CO_2 trapping mineral assemblages are as follows: calcite, dawsonite, and siderite in the Liujiagou formation; calcite and dawsonite in the Shiqianfeng formation; calcite, dawsonite, and magnesite in the Shihezi formation. And calcite, dawsonite, and siderite are stable CO_2 trapping minerals, while dolomite, ankerite, and magnesite are not.

(3) The increase in porosity and permeability of the three formations in the first 100 years is consistent with the observed increasing injectivity at Shenhua CCS Project. The decrease in porosity and permeability after 100 years shows agreement with other modelling studies using the similar methods.

Numerical simulation of geochemical reactions depends on the precision and availability of the equilibrium constants, kinetic parameters, and properties of fluids and host rocks. More work about getting these parameters through experiments should be done. Numerical simulation not limited by time scale can predict a long-term scene. In the future we may have more field data to revise the models and gradually build the big data for CCS. More sensitivity analysis about the mineral assemblages will help to better understand the geochemical reactions. In the current stage, the results in this study have been compared with other studies; they can be useful for the evaluation of long-term CO_2 geological storage and the geochemical process for practical implementations of CCS.

Conflicts of Interest

The authors declare that there are no conflicts of interest regarding the publication of this paper.

Acknowledgments

This work was supported by the National Natural Science Foundation of China (NSFC, Grant no. 41572233) and a bilateral project China Australia Geological Storage of CO_2 Project Phase 2 (CAGS2).

References

[1] World Meteorological Organization, *The Global Climate in 2011–2015*, 2016.

[2] E. Bryant, *Climate process and change*, Cambridge University Press, Cambridge, UK, 1997.

[3] C. J. Jepma and M. Munasinghe, "Climate change policy," in *Jepma CJ Munasinghe M*, p. 331, Cambridge University Press, New York, 1998.

[4] S. Bachu, "Sequestration of CO2 in geological media: Criteria and approach for site selection in response to climate change," *Energy Conversion and Management*, vol. 41, no. 9, pp. 953–970, 2000.

[5] IPCC, *IPCC Special Report on carbon dioxide capture and storage. Prepared by Working Group III of the Intergovernmental Panel on Climate Change*, Cambridge University Press, Cambridge, United Kingdom/New York, NY, USA, 2005.

[6] L. André, P. Audigane, M. Azaroual, and A. Menjoz, "Numerical modeling of fluid-rock chemical interactions at the supercritical CO_2-liquid interface during CO_2 injection into a carbonate reservoir, the Dogger aquifer (Paris Basin, France)," *Energy Conversion and Management*, vol. 48, pp. 1782–1797, 2007.

[7] N. Assayag, J. Matter, M. Ader, D. Goldberg, and P. Agrinier, "Water-rock interactions during a CO2 injection field-test: Implications on host rock dissolution and alteration effects," *Chemical Geology*, vol. 265, no. 1-2, pp. 227–235, 2009.

[8] G. Yang, Y. Li, and A. Atrens, "Reactive transport modelling of long-term CO2 sequestration mechanisms at the Shenhua CCS Demonstration Project," *China. Journal of Earth Science*, vol. 28, no. 3, pp. 457–472, 2016.

[9] S. Bachu and D. B. Bennion, "Experimental assessment of brine and/or CO2 leakage through well cements at reservoir conditions," *International Journal of Greenhouse Gas Control*, vol. 3, no. 4, pp. 494–501, 2009.

[10] P. E. S. Bergmo, A.-A. Grimstad, and E. Lindeberg, "Simultaneous CO2 injection and water production to optimise aquifer storage capacity," *International Journal of Greenhouse Gas Control*, vol. 5, no. 3, pp. 555–564, 2011.

[11] Q. Fang and Y. Li, "Exhaustive brine production and complete CO_2 storage in Jianghan Basin of China," *Environmental Earth Sciences*, vol. 72, no. 5, pp. 1541–1553, 2014.

[12] F. Cipolli, B. Gambardella, L. Marini, G. Ottonello, and M. V. Zuccolini, "Geochemistry of high-pH waters from serpentinites of the Gruppo di Voltri (Genova, Italy) and reaction path modeling of CO2 sequestration in serpentinite aquifers," *Applied Geochemistry*, vol. 19, no. 5, pp. 787–802, 2004.

[13] I. Gaus, M. Azaroual, and I. Czernichowski-Lauriol, "Reactive transport modelling of the impact of CO2 injection on the clayey cap rock at Sleipner (North Sea)," *Chemical Geology*, vol. 217, no. 3-4, pp. 319–337, 2005.

[14] P. Audigane, I. Gaus, I. Czernichowski-Lauriol, K. Pruess, and T. Xu, "Two-dimensional reactive transport modeling of CO2 injection in a saline aquifer at the Sleipner site, North Sea," *American Journal of Science*, vol. 307, no. 7, pp. 974–1008, 2007.

[15] S. Amin, D. J. Weiss, and M. J. Blunt, "Reactive transport modelling of geologic CO2 sequestration in saline aquifers: The influence of pure CO2 and of mixtures of CO2 with CH4 on the sealing capacity of cap rock at 37∘C and 100bar," *Chemical Geology*, vol. 367, pp. 39–50, 2014.

[16] T. Xu, J. A. Apps, and K. Pruess, "Numerical simulation of CO_2 disposal by mineral trapping in deep aquifers," *Applied Geochemistry*, vol. 19, pp. 917–936, 2004.

[17] T. Xu, J. A. Apps, and K. Pruess, "Mineral sequestration of carbon dioxide in a sandstone-shale system," *Chemical Geology*, vol. 217, no. 3-4, pp. 295–318, 2005.

[18] T. Xu, E. Sonnenthal, N. Spycher, and K. Pruess, "TOUGHREACT—A simulation program for non-isothermal multiphase reactive geochemical transport in variably saturated geologic media: Applications to geothermal injectivity and CO_2 geological sequestration," *Computers & Geosciences*, vol. 32, pp. 145–165, 2006.

[19] M. Wigand, J. W. Carey, H. Schütt, E. Spangenberg, and J. Erzinger, "Geochemical effects of CO_2 sequestration in sandstones under simulated in situ conditions of deep saline aquifers," *Applied Geochemistry*, vol. 23, no. 9, pp. 2735–2745, 2008.

[20] Y. Okuyama, M. Sasaki, S. Nakanishi, N. Todaka, and S. Ajima, "Geochemical CO2 trapping in open aquifer storage - the Tokyo Bay model," in *Proceedings of the 9th International Conference on Greenhouse Gas Control Technologies, GHGT-9*, pp. 3253–3258, usa, November 2008.

[21] Y. K. Kharaka, D. R. Cole, S. D. Hovorka, W. D. Gunter, K. G. Knauss, and B. M. Freifeld, "Gas-water-rock interactions in Frio Formation following CO_2 injection: implications for the storage of greenhouse gases in sedimentary basins," *Geology*, vol. 34, no. 7, pp. 577–580, 2006.

[22] S. D. Hovorka, S. M. Benson, C. Doughty et al., "Measuring permanence of CO_2 storage in saline formations: the Frio experiment," *Environmental Geosciences*, vol. 13, no. 2, pp. 105–121, 2006.

[23] I. Hutcheon, M. Shevalier, K. Durocher et al., "Interactions of CO2 with formation waters, oil and minerals and CO2 storage at the Weyburn IEA EOR site, Saskatchewan, Canada," *International Journal of Greenhouse Gas Control*, vol. 53, pp. 354–370, 2016.

[24] X. Wu, *Carbon Dioxide Capture and Geological Storage: The First Massive Exploration in China*, Beijing Science Press, 2013.

[25] H. Wang, *Study on the Interaction of CO2 Fluid with Sandstone in Shiqianfeng*, Jilin University, 2012.

[26] X. Yang, *Experimental study of CO2 fluid on the geological transformation of reservoir sandstone*, Jilin University, 2012.

[27] Y. Tao, *Experimental study on the interaction of CO_2/CO_2-H_2S fluid with sandstone in Liujiagou*, Jilin University, 2013.

[28] Q. Zhu, D. Zuo, and S. Zhang, "Simulation of geomechanical responses of reservoirs induced by CO_2 multilayer injection in the Shenhua CCS project, China," *International Journal of Greenhouse Gas Control*, vol. 42, pp. 405–414, 2015.

[29] Q. Li, G. Liu, X. Liu, and X. Li, "Application of a health, safety, and environmental screening and ranking framework to the Shenhua CCS project," *International Journal of Greenhouse Gas Control*, vol. 17, pp. 504–514, 2013.

[30] K. Zhang, J. Xie, C. Li, L. Hu, X. Wu, and Y. Wang, "A full chain CCS demonstration project in northeast Ordos Basin, China: Operational experience and challenges," *International Journal of Greenhouse Gas Control*, vol. 50, pp. 218–230, 2016.

[31] T. Xu, N. Spycher, EL. Sonnenthal, L. Zheng, and K. Pruess, "TOUGHREACT Users Guide: A simulation program for non-isothermal multiphase reactive transport in variably saturated geologic media," *Version*, vol. 2.0, 2012.

[32] H. Tian, *Impacts of CO2-brine-rock interaction on the caprock sealing efficiency: A case study of Shiqianfeng formation mudstone caprock in Ordos Basin*, Jilin University, 2014.

[33] W. Zhang, Y. Li, and T. Xu, "Long-term variations of CO_2 trapped in different mechanisms in deep saline formations: A case study of the Songliao Basin, China," *International Journal of Greenhouse Gas Control*, vol. 3, no. 2, pp. 161–180, 2009.

[34] A. C. Lasaga, J. M. Soler, J. Ganor, T. E. Burch, and K. L. Nagy, "Chemical weathering rate laws and global geochemical cycles," *Geochimica et Cosmochimica Acta*, vol. 58, no. 10, pp. 2361–2386, 1994.

[35] I. Gaus, P. Audigane, L. André et al., "Geochemical and solute transport modelling for CO2 storage, what to expect from it?" *International Journal of Greenhouse Gas Control*, vol. 2, no. 4, pp. 605–625, 2008.

[36] A. Credoz, O. Bildstein, M. Jullien et al., "Experimental and modeling study of geochemical reactivity between clayey caprocks and CO2 in geological storage conditions," in *Proceedings of the 9th International Conference on Greenhouse Gas Control Technologies, GHGT-9*, pp. 3445–3452, usa, November 2008.

[37] M. T. van Genuchten, "A closed-form equation for predicting the hydraulic conductivity of unsaturated soils," *Soil Science Society of America Journal*, vol. 44, no. 5, pp. 892–898, 1980.

[38] A. T. Corey, "The interrelation between gas and oil relative permeabilities," in *Producers Monthly*, pp. 38–41, Producers Monthly, 1954.

[39] J. Chen and Z. Zheng, *Probability and Statistics*, Peking University Press, Beijing, China, 2015.

[40] G. Yang, Y. Li, and X. Ma, "Effect of chlorite on CO2-water-rock interaction," *Earth ScienceJournal of China University of Geosciences*, vol. 39, no. 4, 2014.

[41] K. Wang, T. Xu, H. Tian, and F. Wang, "Impacts of mineralogical compositions on different trapping mechanisms during long-term CO_2 storage in deep saline aquifers," *Acta Geotechnica*, vol. 11, no. 5, pp. 1167–1188, 2016.


Journal of
Geochemistry

Scientifica

International Journal of
Ecology
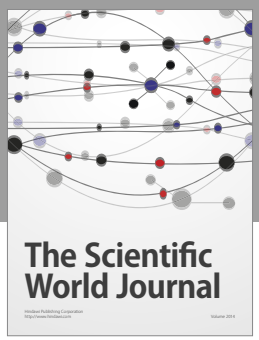
The Scientific
World Journal
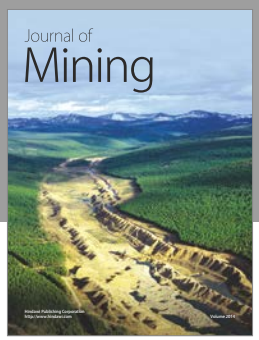
Journal of
Mining

Journal of
Earthquakes

Paleontology Journal
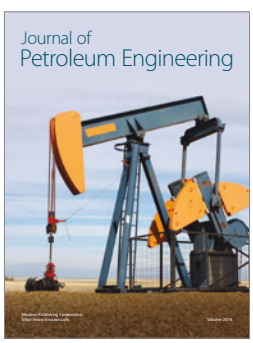
Journal of
Petroleum Engineering

Hindawi
Submit your manuscripts at
https://www.hindawi.com
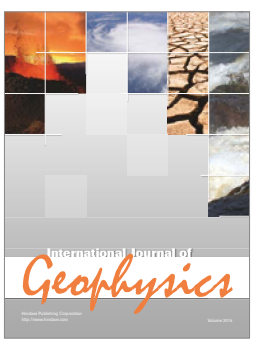
International Journal of
Geophysics
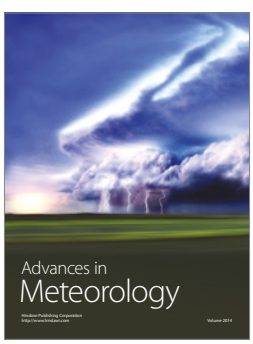
Advances in
Meteorology

Journal of
Climatology
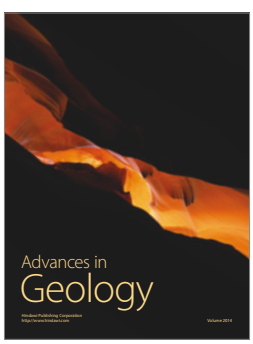
Advances in
Geology
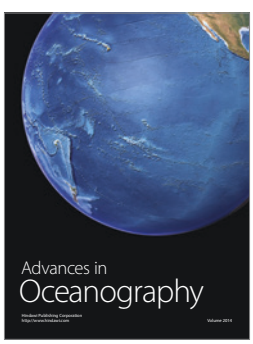
Advances in
Oceanography
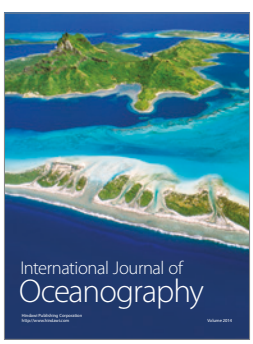
International Journal of
Oceanography
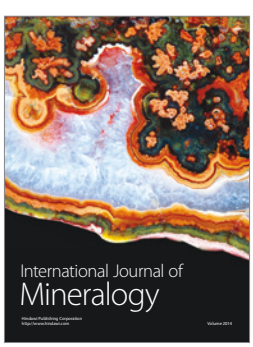
International Journal of
Mineralogy

Journal of
Geological Research

International Journal of
Atmospheric Sciences

Applied &
Environmental
Soil Science
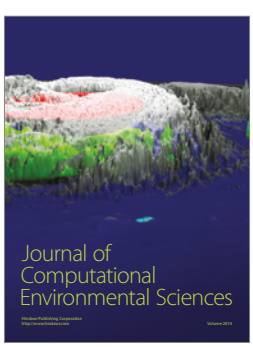
Journal of
Computational
Environmental Sciences